Synthesis of sandwich-like TiO₂@C composite hollow spheres with high rate capability and stability for lithium-ion batteries

Lichen Liu [a,c,1], Qi Fan [b,1], Chuanzhi Sun [d], Xianrui Gu [a,c], Hao Li [a,c], Fei Gao [c], Yanfeng Chen [b,**], Lin Dong [a,c,*]

[a] Key Laboratory of Mesoscopic Chemistry of Ministry of Education, School of Chemistry and Chemical Engineering, Nanjing University, Nanjing 210093, PR China
[b] College of Engineering and Applied Science, National Lab of Solid State Microstructures, Nanjing University, Nanjing 210093, PR China
[c] Jiangsu Key Laboratory of Vehicle Emissions Control, Center of Modern Analysis, Nanjing University, Nanjing 210093, PR China
[d] Department of Chemistry, Chemical Engineering and Materials Science, Shandong Normal University, Jinan 250014, PR China

HIGHLIGHTS

► Sandwich-like TiO₂@C hollow spheres with {001} facets exposed are obtained.
► TiO₂ shells are wrapped in electron-conductive carbon layers.
► TiO₂@C hollow spheres show superior rate capability and stability.

GRAPHICAL ABSTRACT
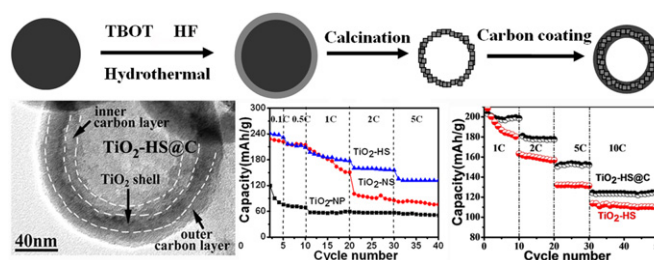
ABSTRACT

Novel sandwich-like TiO₂@C composite hollow spheres with {001} facets exposed are obtained through hydrothermal carbon-coating treatment for the first time. Based on investigations by transmission electron microscopy (TEM), scanning electron microscopy (FESEM), XRD, laser Raman spectra, and N₂ adsorption–desorption isotherms, TiO₂ shells are proved to be wrapped in porous carbon layers, which provide conductive support for TiO₂, resulting the improvement in electronic conductivity and diffusion of Li$^+$. Moreover, these TiO₂ shells expose the reactive {001} facets, which facilitate Li$^+$ insertion/extraction. Through combining the above advantages, TiO₂@C composite hollow spheres show more superior rate capability and higher stability than TiO₂ nanoparticles (Degussa P25), TiO₂ nanosheets with {001} facets exposed, and TiO₂ hollow spheres before carbon-coating. This method may be extended to synthesize other sandwich-like composite hollow spheres for energy storage.

© 2012 Elsevier B.V. All rights reserved.

1. Introduction

The demands for rechargeable batteries are increasing in power sources both of portable electronic equipment and automobile electrical systems. Among various candidate power systems, lithium-ion batteries have attracted much attention because of their high energy storage density, long cycle life, little memory effect, poisonous metals free [1,2]. Crystalline TiO₂ has attracted much attention in recent years because of its excellent physico-chemical properties and potential application in lithium-ion

* Corresponding author. Jiangsu Key Laboratory of Vehicle Emissions Control, Center of Modern Analysis, Nanjing University, Hankou Road 22#, Nanjing 210093, PR China. Tel.: +86 25 8359 2290; fax: +86 25 8331 7761.
** Corresponding author. Fax: +86 25 8621 2844.
E-mail addresses: yfchen@nju.edu.cn (Y. Chen), donglin@nju.edu.cn (L. Dong).
[1] These authors contributed equally to this work.

batteries. With low cost and high stability, TiO_2 has been regarded as a promising substitute for graphite that used in the present commercial lithium-ion batteries [3,4]. However, due to the poor electronic conductivity and low diffusion rate of Li^+, the electrochemical performance of TiO_2 electrode materials is limited [5]. Therefore numerous TiO_2 nanostructures and TiO_2 based nanocomposites have been synthesized to increase the lithium exchange efficiency, specific capacity and cyclability [6–10].

Hollow structures have attracted great attention in Li-ion batteries for their improvement in reversible lithium storage capabilities [11,12]. The hollow structure may provide extra active sites, large surface area and reduced effective diffusion distance for lithium ions, which is beneficial for better specific capacity and rate capability [13]. In the past few years, TiO_2 hollow spheres have been prepared for Li-ion batteries through different methods. Song et al. prepared anatase TiO_2 hollow spheres through a one-step template free method [14]. While Wang et al. reported a sol–gel process using hard templates to fabricate TiO_2 hollow spheres [15]. They both found the TiO_2 hollow spheres showed better electrochemical properties compared to TiO_2 nanoparticles.

Except for synthesizing hollow structures, the exposed facets also have a significant influence on the Li^+ diffusion efficiency. Several theoretical studies have pointed out that due to the special crystal structure of anatase, Li^+ insertion/extraction will be probably facilitated through the {001} facets. Anatase TiO_2 nanosheet with {001} facets exposed have been proved to be an ideal host structure for fast and efficient lithium insertion/extraction [16,17]. In order to obtain stable architectures, several hierarchical TiO_2 nanostructures with {001} facets exposed have also been fabricated and show excellent performance in the Li-ion batteries. Lou and his co-workers have synthesized TiO_2 hollow spheres with {001} facets exposed, which exhibit fast reversible lithium storage [18,19].

The above two strategies mainly try to control the topological structures or exposed crystal facets to optimize the capability of TiO_2 anode materials. Another alternative approach to overcome the disadvantages in TiO_2 based materials for Li-ion batteries is using nanocomposite materials. In particular, nanopainting with carbon has recently been found effective for improving cyclability and electronic conductivity [20]. Kelder et al. synthesized carbon-coated TiO_2 nanoparticles using phenyl phosphonic acid followed by special thermal treatments, which showed an improvement in electronic conductivity. What's more, the carbon layer can work as a buffer to mitigate the mechanical stress caused by Li^+ insertion and extraction [21,22].

Combining the nanostructure design of electrode materials and the nanocomposite concept, we herein report a new hierarchical anode nanostructure: sandwich-like TiO_2@carbon composite hollow spheres with anatase TiO_2 {001} facets exposed (denoted as TiO_2-HS@C). The TiO_2-HS@C was synthesized through a two-step coating process as showed in Scheme 1. Uniform carbon spheres were obtained by hydrothermal treatment of glucose with the addition of CTAB (TEM image is presented in Fig. S1). Then precursor of TiO_2 was coated on carbon spheres in the presence of HF to control the exposed facets of anatase TiO_2. Afterward, TiO_2 hollow spheres with {001} facets exposed (denoted as TiO_2-HS) were obtained through the removal of the carbon cores. The carbon layers were then coated on the shells of TiO_2 hollow spheres by the pyrolysis of glucose under hydrothermal conditions. Finally, the

products were dried and heat-treated under N_2 atmosphere to carbonize the carbon precursors, to produce the sandwich-like TiO_2-HS@C.

Compared to commercial TiO_2 nanoparticles (Degussa P25), the TiO_2 nanosheets with {001} facets exposed (denoted as TiO_2-NS, synthesized according to the work of Xie et al. [23]) and TiO_2 hollow spheres without carbon-coating (TiO_2-HS), these TiO_2@C composite hollow spheres show larger specific capacity, much better rate capability and higher cyclability. In this article, we will discuss the relation between the structural characteristics and electrochemical performance.

2. Experiment section

2.1. Materials preparation

All the reagents were of analytical grade and were used without further purification.

2.1.1. Synthesis of carbon spheres
Carbon spheres were synthesized by a previously reported method [24]. In a typical synthesis, 2.87 g glucose and 0.2 g cetyl-trimethyl ammonium bromide (CTAB) were dissolved in 30 mL distilled water to for an aqueous solution. Then the solution was placed in a 50-mL teflon-lined stainless steel autoclave, and maintained at 180 °C for 9 h in an air-flow electric oven. After the hydrothermal treatment, it was allowed to cool naturally to room temperature. The solid brown product was collected by centrifuging at 7000 rpm for 10 min, and washed with ethanol and water for three times, respectively. Finally, the obtain product was dried in air at 80 °C for 6 h.

2.1.2. Synthesis of TiO_2 hollow spheres with {001} facets exposed (TiO_2-HS)
TiO_2 hollow spheres with {001} facets exposed (TiO_2-HS) were prepared through the following method. For a typical procedure, 0.2 g carbon spheres were dispersed in 30 mL ethanol with the assistance of ultrasound. Then 0.34 mL $Ti(OC_4H_9)_4$ (TBOT) was added to the black suspension, and dispersed under ultrasound. Subsequently, a solution including 10 mL ethanol, 0.75 mL hydrofluoric acid solution (with a concentration ca. 47 wt.%) and 0.25 mL distilled water was dropped to the suspension under stirring. After the addition of HF, the mixture was kept stirring for 6 h at room temperature, after which it was transferred to a 50-mL teflon-lined stainless steel autoclave. Then it was maintained at 180 °C for 24 h in an air-flow electric oven. After cooling to room temperature, The product was collected by centrifuging at 7000 rpm for 10 min, and washed with ethanol and water for three times, respectively. Afterward, it was dried in air at 80 °C for 6 h. The final products were obtained after calcination at 500 °C in flowing air for 4 h with a heating rate of 2 °C min^{-1}, resulting the formation of TiO_2-HS.

2.1.3. Synthesis of sandwich-like TiO_2@carbon composite hollow spheres (TiO_2-HS@C)
In order to improve the cyclability and rate capability of TiO_2-HS, we have prepared TiO_2@carbon composite hollow spheres. In a typical synthesis, 0.1 g of as-synthesized TiO_2-HS sample was
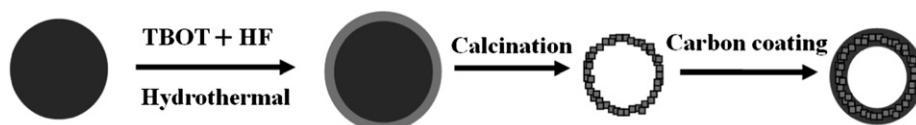
Scheme 1. Schematic illustration of the synthesis process of TiO_2 hollow spheres and TiO_2@C sandwich-like hollow spheres.

dispersed by ultrasonication in 30 mL of 0.5 M aqueous glucose solution. The suspension was transferred to a 50-mL teflon-lined autoclave, which was then heated in an air-flow electric oven at 180 °C for 3 h. The product was again harvested by centrifugation and washed with deionized ethanol and distilled water for three times, respectively. After drying at 80 °C for 6 h, the resulting brown powder was carbonized at 550 °C for 3 h under inert atmosphere to obtain TiO_2@carbon composite hollow spheres.

2.2. Materials characterization

Transmission electron microscopy (TEM) images were taken on a JEM-2100 instrument at an acceleration voltage of 200 kV. The samples were crushed and dispersed in A.R. grade ethanol and the resulting suspensions were allowed to dry on carbon film supported on copper grids.

Field-emission scanning electron microscopy (FESEM) images were observed by a Hitachi S-4800 instrument at an acceleration voltage of 10 kV.

X-ray diffraction (XRD) measurement patterns were recorded on a Philips X'pert Pro diffractometer using Ni-filtered Cu Kα1 radiation ($\lambda = 0.15,408$ nm). The X-ray tube was operated at 40 kV and 40 mA.

Raman spectra were recorded by using Renishaw in via spectrometer. Raman excitation at 514.5 nm was provided by Ar$^+$ laser. A laser power of 20 mW at the sample was applied.

The thermogravimetric analysis (TGA) was carried out under an air flow of 60 mL min^{-1} using TA Instruments Q500 from room temperature to 550 °C with a heating rate of 5 °C min^{-1}.

Brunauer−Emmet−Teller (BET) surface areas were measured by nitrogen adsorption at 77 K on a Micrometrics ASAP-2020 adsorption apparatus. Before each adsorption measurement, approximate 0.15 g of a catalyst sample was degassed in a N_2/He mixture at 300 °C for 4 h. The BET surface area was determined by a multipoint BET method using the adsorption data in the relative pressure (P/P_0) range 0.05−0.3. Desorption isotherm was used to determine the pore size distribution via the Barret−Joyner−Halender (BJH) method. The nitrogen adsorption volume at the relative pressure (P/P_0) of 0.994 was used to determine the pore volume and average pore size.

2.3. Electrochemical measurement

The electrochemical measurements were carried out using homemade two-electrode Swagelok-type cells with lithium metal as the counter and reference electrodes at room temperature. The working electrode (diameter = 10 mm) was prepared by mixing the active materials with carbon black and PTFE in a weight ratio of 8:1:1 for electrochemical testing. The tap density of TiO_2-NP, TiO_2-NS, TiO_2-HS and TiO_2-HS@C is 0.90 g cm^{-3}, 0.81 g cm^{-3}, 0.65 g cm^{-3} and 0.75 g cm^{-3}, respectively.

The cells were assembled in Ar-filled glove box with the as-prepared working electrode; a Li counter; a separator (Celgard polymer) saturated with a 1 mol L^{-1} LiPF$_6$ solution in ethylene carbonate and dimethyl carbonate (1:1, v/v). Charge−discharge experiments were performed in Land battery cycler over a voltage of 5 mV−3 V (Land Instruments, China).

The EIS measurements were carried out on a CHI660C potentiostat/galvanostat (Shanghai Chenhua Technology Inc., China). The electrodes typically had an active material content of 6−8 mg, as the working electrode. Lithium foil served as the counter and reference electrodes. The impedance spectra were recorded with the help of ZPlot/ZView software under an ac perturbation signal of 5 mV over the frequency range of 1 MHz−100 mHz.

3. Results and discussion

We first employ field-emission scanning electron microscopy (FESEM) and transmission electron microscopy (TEM) to examine the structure and morphology of TiO_2-HS. From the FESEM image (Fig. 1a) we can find that the sample is composed of nanospheres with rough surface. The broken spheres reveal that the nanospheres appear as hollow interior. The hollow structures can be further confirmed by the TEM images. Fig. 1b shows that the hollow spheres have a diameter ranging from 80 to 160 nm, with a ca. 20 nm-thick wall as presented in Fig. 1c. The selected-area electron diffraction (SAED) pattern (Fig. 1d) matches well with that of typical anatase TiO_2, which further confirms that anatase TiO_2 hollow spheres have been prepared using carbon spheres as hard templates.

Recently, anatase TiO_2 nanocrystals with {001} facets exposed have attracted great attention because of their superior physical and chemical properties [16,17]. In the synthesis procedure for TiO_2-HS, we have introduced HF to control the exposed facets of anatase to obtain the active crystal facets. In Fig. 1e, the interplanar crystal spacing 0.235 nm corresponds to anatase {001} facets. Furthermore, observed through the [111] zone axis, the HRTEM image in Fig. 1f displays (101) and (011) crystal facets with an interfacial angle of 82.4°, which is quite consistent with the theoretical value. The insert image shown in Fig. 1f gives the corresponding fast Fourier transform pattern (FFT) of the anatase nanocrystal [25]. Based on the above results, it can be indicated that the as-prepared TiO_2 hollow spheres show the active {001} facets. According to previous reports, Raman spectra can be used to quantify the amount of {001} facets in anatase TiO_2 due to the different surface structures of different crystal facets [26]. The Raman spectrum of TiO_2-HS is showed in Fig. S2. It is estimated that the percentage of the {001} facets is around 33%, which is evidently higher than that in conventional anatase nanoparticles [27].

For the purpose of improving the rate capability and cyclability, we have prepared carbon-coated TiO_2 hollow spheres (TiO_2-HS@C). The morphology of TiO_2-HS@C and microstructures are investigated by FESEM and TEM as shown in Fig. 2. From the FESEM image in Fig. 2a, it can be seen that the spherical structures are preserved after the carbon-coating process. Comparing the FESEM images in Figs. 1a and 2a, one obvious difference can be distinguished: TiO_2-HS seems vague, while TiO_2-HS@C is clear. This phenomenon suggests that the conductive properties of TiO_2-HS have been obviously improved after carbon-coating. In addition, the TEM image (Fig. 2b) suggest that these composite spheres are composed of hollow interior (70−150 nm) and smooth layer (ca. 40 nm). From the magnified TEM image (Fig. 2c), it can be figured out that the TiO_2 shell was wrapped in the inner and outer carbon layers, which seems to be a sandwich-like structure. This sandwich-like construction will provide a conductive support for TiO_2 shell, leading to the improvement in electrochemical performance. Moreover, the diffraction pattern of TiO_2-HS@C (Fig. 2d) appears as poor crystallinity, which implies the formation of a perfect carbon layer. The above results indicate the hydrothermal treatment is efficient to fabricate carbon layers coated TiO_2 hollow spheres.

XRD is performed to investigate the phase structures of TiO_2-HS and TiO_2-HS@C. In Fig. 3, it can be seen that both the samples show typical diffraction patterns of anatase TiO_2 (JCPDS No. 21-1272; space group $I41/amd$ (No. 141)). No other peaks have been observed. These results indicate that the carbon-coating process does not change the phase structure of TiO_2-HS. It should be noted that, the peaks in TiO_2-HS@C become slightly sharper, which implies that the crystallinity of TiO_2 nanoparticles will improve in the carbonization process at 550 °C [28].
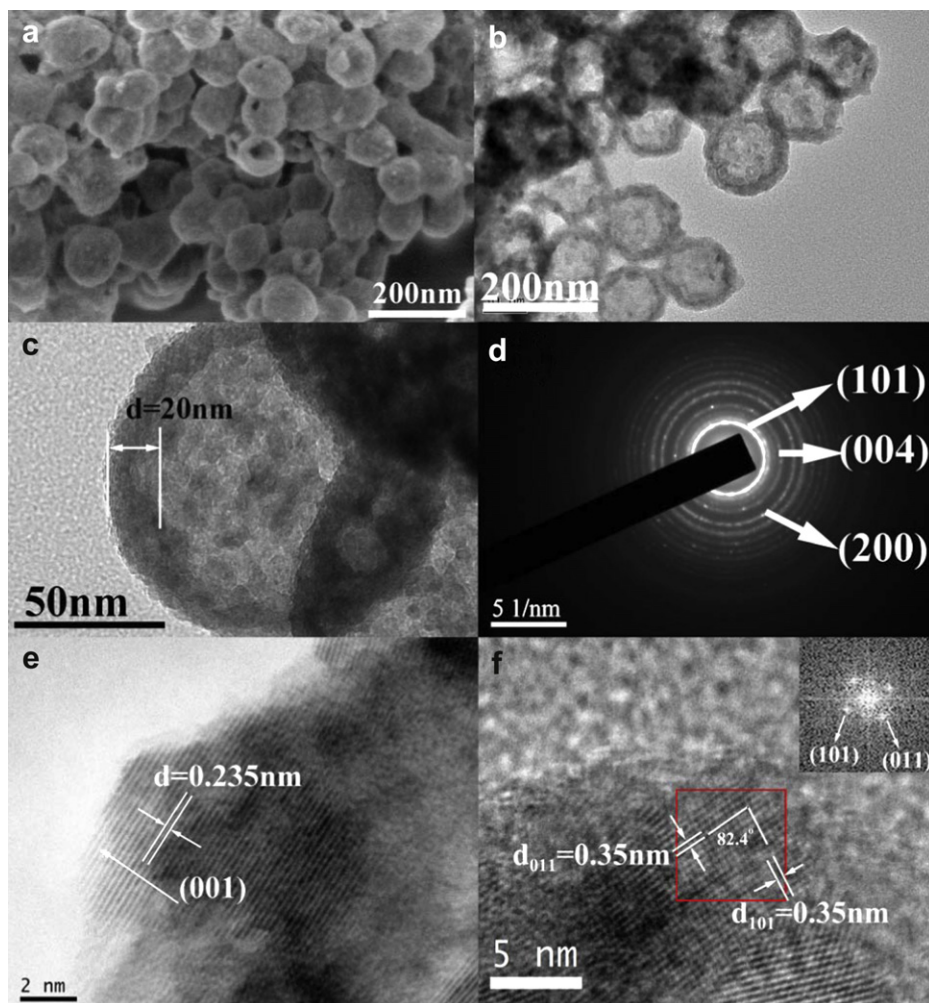
Fig. 1. Morphology characterizations of TiO$_2$-HS. (a) FESEM image; (b) TEM image; (c) magnified TEM image of a single TiO$_2$ hollow sphere; (d) Selective Area Electron Diffraction (SAED) pattern; (e−f) HRTEM image of the TiO$_2$ nanoparticles in TiO$_2$-HS. The insert in (f) shows the corresponding fast Fourier transformation (FFT) pattern.
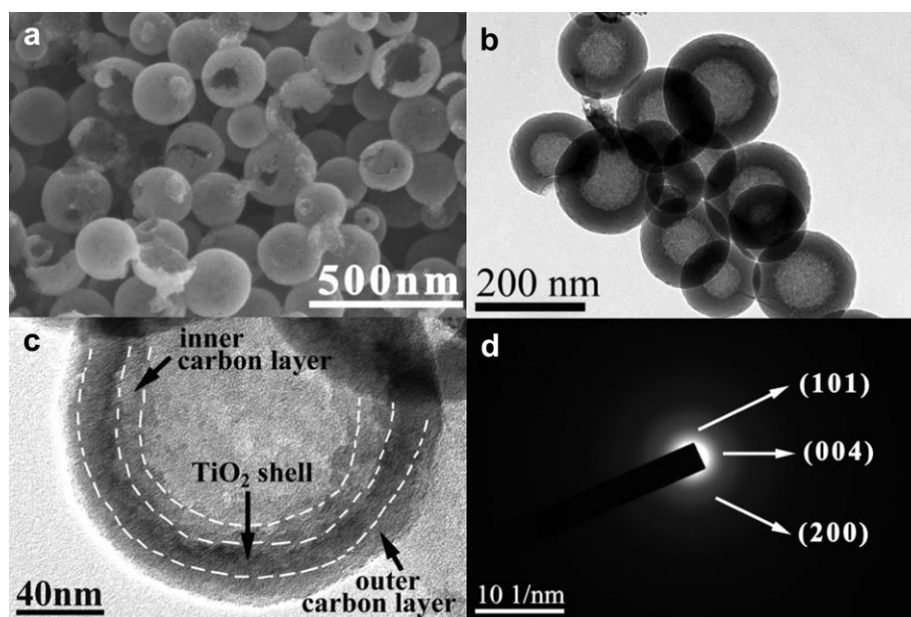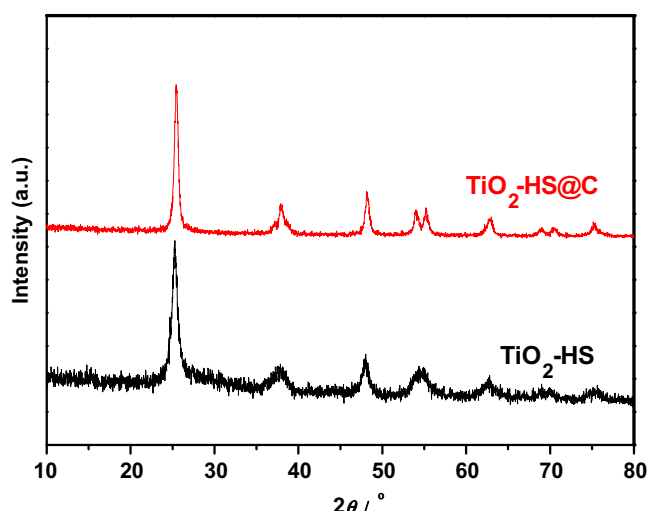

Fig. 2. Morphology characterizations of TiO$_2$-HS@C. (a) FESEM image; (b) TEM image; (c) magnified TEM image of a single TiO$_2$-HS@C sandwich-like hollow spheres; (d) Selective Area Electron Diffraction (SAED) pattern.

Fig. 3. XRD patterns of TiO$_2$-HS and TiO$_2$-HS@C.

To examine the ordering of the carbon layer in TiO$_2$-HS@C, the samples were characterized by Raman spectroscopy (Fig. 4). Both TiO$_2$-HS and TiO$_2$-HS@C show typical Raman features of anatase TiO$_2$ [29], which indicates carbon-coating didn't change the phase type of TiO$_2$-HS. It can be seen that, the intensity of the Raman modes corresponding to anatase TiO$_2$ in TiO$_2$-HS@C is much weaker than that in TiO$_2$-HS. The reason may be that the carbon layer coated on TiO$_2$-HS in the sample TiO$_2$-HS@C will weaken the Raman signal of TiO$_2$, which verifies the formation of well-coated carbon layer. The characteristic peak located at about 1357 cm^{-1} in the Raman spectroscopy of TiO$_2$-HS@C corresponds to the *D* band of carbon, suggesting the disordered carbon. While the peak at about 1586 cm^{-1} corresponds to *G* band of carbon, indicating the existence of sp^2 graphite carbon. It should be noted that, the *G* band of the TiO$_2$-HS@C sample shifted to higher wave numbers compared to the single crystal of graphite (1575 cm^{-1}). This is probably due to the formation of thin carbon shell [30]. The dimensional ratio of the *G* band to the *D* band for the TiO$_2$-HS@C was estimated to be about 1.41, which indicates the formation of a reasonable degree of graphitization [31,32]. These carbon shells will provide as a well conductive medium to improve the conductivity of TiO$_2$-HS. In accordance with the TEM analysis, the
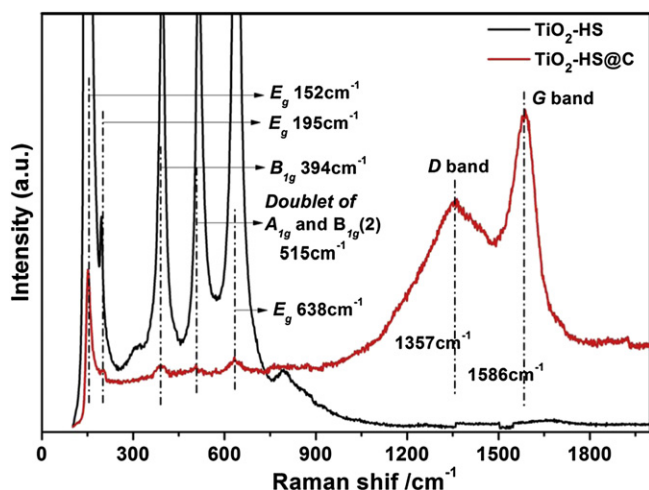
Raman results confirm that a carbon layer has formed in TiO$_2$-HS@C. In order to quantify the weight percentage of carbon in TiO$_2$-HS@C, the as-prepared samples were analyzed by TGA. The TG curves of TiO$_2$-HS and TiO$_2$-HS@C are presented in Fig. S3. The amount of carbon in TiO$_2$-HS@C can be determined by the difference value of the mass loss of the TiO$_2$-HS and TiO$_2$-HS@C, namely 7.3%.

N$_2$ adsorption–desorption isotherms were employed to investigate the possible porous structures of TiO$_2$-HS and TiO$_2$-HS@C, and the results are showed in Fig. 5a. Both the isotherms corresponding to TiO$_2$-HS and TiO$_2$-HS@C are type IV (BDDT classification) with hysteresis loops at high relative pressure, suggesting the presence of mesopores (2–50 nm) and macropores (>50 nm). The shape of the hysteresis loop is type H3, suggesting narrow slit-shaped pores that are probably generated by the porous shells in TiO$_2$-HS [33]. During the carbon-coating process, carbon will fill the pores in TiO$_2$-HS, which can be confirmed by the decrease of pore volume in TiO$_2$-HS@C. Moreover, the corresponding pore size distribution results (Fig. 5b) also verify the above detection according to the narrower pore size distribution in TiO$_2$-HS@C. As to the TiO$_2$-HS@C, the hysteresis loop is type H4, which corresponds to incommodious pore canals. It's very interesting to figure out that the BET surface area of TiO$_2$-HS@C (139 m^2 g^{-1}) is much higher than that of TiO$_2$-HS (66 m^2 g^{-1}). From the broken carbon
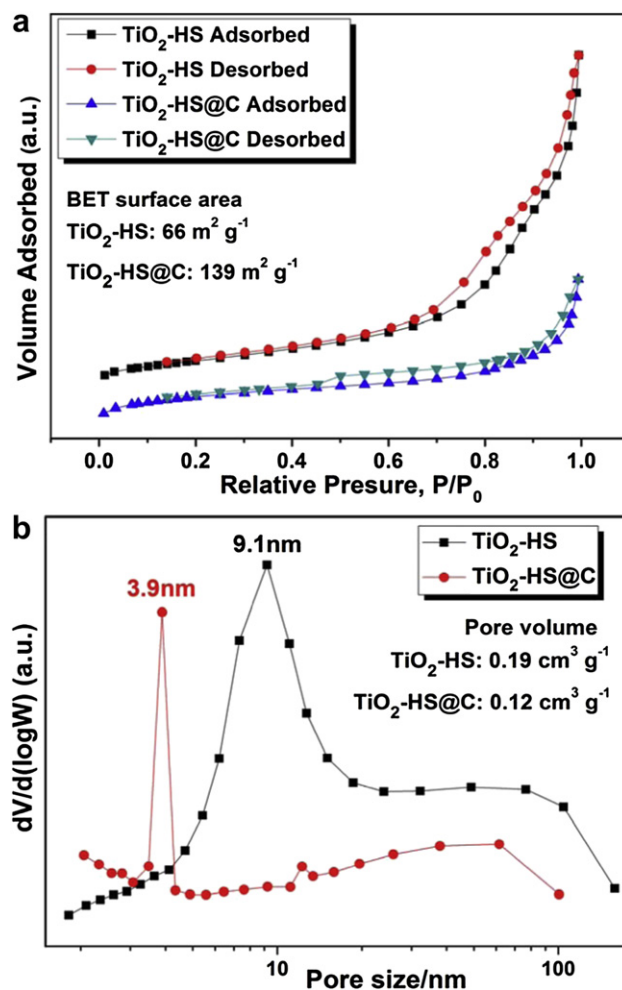
Fig. 5. (a) N$_2$ adsorption/desorption isothermals of TiO$_2$-HS and TiO$_2$-HS@C; (b) size distributions of TiO$_2$-HS and TiO$_2$-HS@C. The specific surface areas and pore volumes are also presented.

Fig. 4. Raman spectra of TiO$_2$-HS and TiO$_2$-HS@C.

layers in TiO_2-HS@C (Fig. S4), we can figure out that the carbon shells show porous structures, which may lead to the increase in BET surface area and the transformation of the type of hysteresis from H3 to H4 [34]. These small pore canals will provide effective diffusion channels for Li^+ in the charge/discharge process, which may be helpful for improving the diffusion of Li^+.

To examine the influences of structural differences in the electrochemical properties of those TiO_2-based electrode materials, the Li-ion insertion/extraction properties in the TiO_2-HS, TiO_2 nanosheets with {001} facets exposed (TiO_2-NS, TEM images can be seen in Fig. S5) and commercial TiO_2 nanoparticles (Degussa P25, denoted as TiO_2-NP) were investigated, respectively. Fig. 6a shows the charge–discharge curves of TiO_2-NP at 0.1 C at the activation process. The battery with this electrode shows an obvious capacity loss in this process: the first discharge capacity is 190 mA h g^{-1} while the fifth discharge capacity is 80 mA h g^{-1}, suggesting an irreversible capacity loss of 58%. This fast capacity loss may be caused by the irreversibly inserted lithium ions in TiO_2 nanoparticles at the first stage of charge–discharge process [14]. As for TiO_2-NS (Fig. 6b) and TiO_2-HS (Fig. 6c), they show relatively stable capacities compared to TiO_2-NP since the capacity loss in the activation process is less than 10%. Both samples show a moderate capacity more than 210 mA h g^{-1} after five cycles.

Fig. 6d shows the cycling performance of the above three electrodes at various current rates. Clearly, caused by the fast irreversible capacity loss in the starting stage, TiO_2-NP shows the poorest rate capacity (only 50–60 mA h g^{-1} at 5 C) due to its solid and disorder structures. In addition, the rate capacity of TiO_2-NS is a little higher than that of TiO_2-NP (about 70 mA h g^{-1} at 5 C), which can be ascribed to the highly efficient solid-state diffusion of Li^+ ions through the {001} facets [16,17]. Remarkably, the TiO_2-HS electrode has the best capacity retentions at different C rates (161 mA h g^{-1} at 2 C, 133 mA h g^{-1} at 5 C) compared to TiO_2-NP and TiO_2-NS. This significant improvement in rate capability can be contributed to the combination of the hollow architecture and {001} facets exposed in TiO_2-HS. Based on the above experimental

results and analysis, we can conclude that through building hollow spheres with {001} facets exposed can optimize electrochemical performance of TiO_2 electrode materials.

TiO_2-HS@C was designed to reform the conductivity and stability of TiO_2-HS electrode, so as to further improve rate capability and cyclic retention. Fig. 7a, b shows the charge–discharge voltage profiles of TiO_2-HS@C and TiO_2-HS electrode at various current rates. The rate-capacity of TiO_2-HS@C electrode is obviously better than that of TiO_2-HS. It shows a large capacity as 196 mA h g^{-1} at 1 C, 178 mA h g^{-1} at 2 C and 153 mA h g^{-1} at 5 C. Even at a current rate of as high as 10 C (2000 mA h g^{-1}), the sandwich-like TiO_2-HS@C are still able to deliver a reversible capacity of 125 mA h g^{-1}. While the TiO_2-HS electrode shows relatively poor capacities: 180 mA h g^{-1}, 161 mA h g^{-1}, 132 mA h g^{-1} and 110 mA h g^{-1} at the discharge rates of 1, 2, 5 and 10 C.

In order to understand the improved high-rate performance of TiO_2-HS@C, the impedance spectra of TiO_2-HS@C and TiO_2-HS were characterized. As displayed in Fig. 7c, the EIS spectrum of both TiO_2-HS and TiO_2-HS@C consist of one semicircle in the high-frequency region and a line in the low-frequency region. To further understand the electrochemical processes, these two spectra are fit and analyzed by ZsimpWin software. The proposed model of the equivalent circuit and fitted parameters are shown in Fig. S6 and Table S1. Comparing the fitted impedance parameters in Table S1, we can figure out that R_Ω, Rs and R_{ct} of TiO_2-HS@C show a significant decrease compared to those of TiO_2-HS, which infers the improvement of charge carrier transport caused by carbon-coating [35]. Especially, the R_{ct} in TiO_2-HS@C is much smaller than that of TiO_2-HS, which indicates the good electrical contact among the TiO_2-HS@C hollow spheres. Therefore, according to the EIS analysis, both electron-transport and Li^+ diffusion of TiO_2-HS@C electrode are obviously optimized compared to TiO_2-HS electrode [36,37]. It can be mainly ascribed to the well-coated carbon shell, which can provide additional structural support and high electronic conductivity of TiO_2-HS [38]. Cycling performance of TiO_2-HS and TiO_2-HS electrodes at 1 C–10 C were shown as Fig. 7d. The TiO_2-HS@C
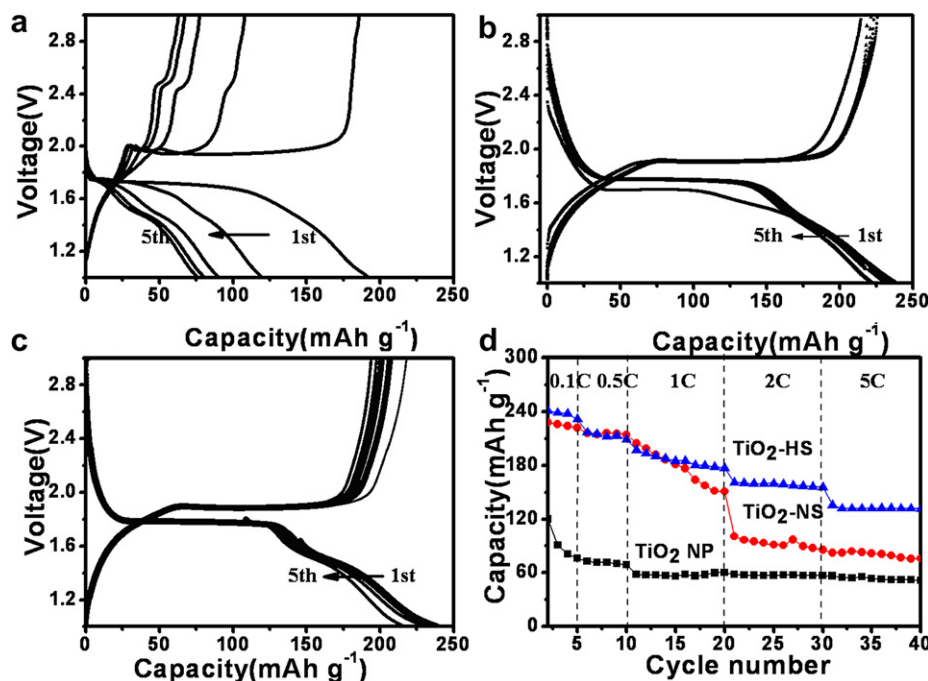

Fig. 6. Discharge/charge profiles of different TiO_2 electrode materials: (a) TiO_2 nanoparticles (TiO_2-NP); (b) TiO_2 nanosheets (TiO_2-NS); (c) TiO_2-HS. (d) Cycling performances of TiO_2-NP, TiO_2 nanosheets and TiO_2-HS.

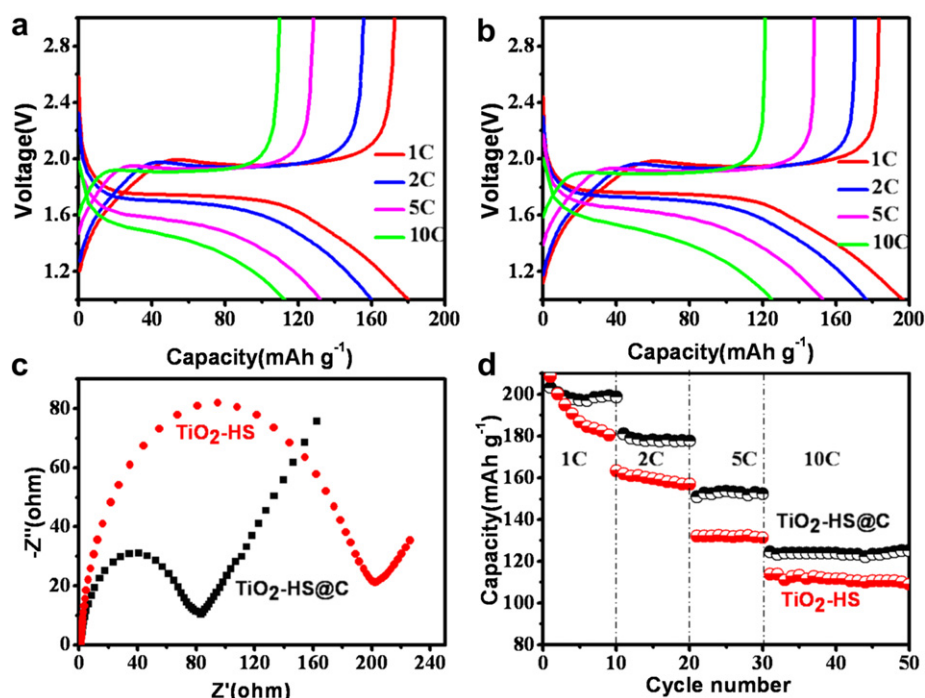**Fig. 7.** Discharge/charge profiles under at various C rates: (a) TiO$_2$-HS; (b) TiO$_2$-HS@C. (c) Electrochemical impedance spectra of TiO$_2$-HS and TiO$_2$-HS@C electrodes. (d) Capacity retention performances of TiO$_2$-HS and TiO$_2$-HS@C at various C rates.

display good capacity retentions at different C rates, which is better than TiO$_2$-HS. Furthermore, TiO$_2$-HS@C show better electrochemical performance compared to other TiO$_2$ hollow structures reported recently [18,19,39,40]. Therefore, with the rational carbon-coating, TiO$_2$-HS@C exhibit better rate capability and stability, which can be ascribed to the novel sandwich-like hierarchical structures.

4. Conclusions

In this work, novel sandwich-like TiO$_2$@C composite hollow spheres with {001} facets exposed were obtained through hydrothermal carbon-coating treatment for the first time. Based on the characterizations, TiO$_2$ shells were proved to be wrapped in porous carbon layers, which provide conductive support for TiO$_2$. Moreover, these TiO$_2$ shells expose the reactive {001} facets, which facilitate Li$^+$ insertion/extraction. These structural features significantly optimize the electrochemical performance of TiO$_2$ electrode in lithium-ion batteries during the charge/discharge process. Through combining the above advantages, TiO$_2$@C composite hollow spheres show more superior rate capability and higher stability than TiO$_2$ nanoparticles (Degussa P25), TiO$_2$ nanosheets with {001} facets exposed, and TiO$_2$ hollow spheres without carbon-coating. This method may be extended to synthesize other sandwich-like composite hollow spheres for energy storage.

Acknowledgements

Appendix A. Supplementary data

Supplementary data related to this article can be found at http://dx.doi.org/10.1016/j.jpowsour.2012.07.105.

References

[1] M. Armand, J.-M. Tarascon, Nature 451 (2008) 652–657.
[2] J.B. Goodenough, Y. Kim, Chem. Mater. 22 (2010) 587–603.
[3] L. Kavan, M. Kalbac, M. Zukalova, I. Exnar, V. Lorenzen, R. Nesper, M. Graetzel, Chem. Mater. 16 (2004) 477–485.
[4] U. Lafont, D. Carta, G. Mountjoy, A.V. Chadwick, E.M. Kelder, J. Phys. Chem. C 114 (2010) 1372–1378.
[5] Z. Yang, D. Choi, S. Kerisit, K.M. Rosso, D. Wang, J. Zhang, G. Graff, J. Liu, J. Power Sources 192 (2009) 588–598.
[6] D. Deng, M.G. Kim, J.Y. Lee, J. Cho, Energy Environ. Sci. 2 (2009) 818.
[7] X. Su, Q. Wu, X. Zhan, J. Wu, S. Wei, Z. Guo, J. Mater. Sci. 47 (2011) 2519–2534.
[8] L. Shen, X. Zhang, H. Li, C. Yuan, G. Cao, J. Phys. Chem. Lett. 2 (2011) 3096–3101.
[9] F.-F. Cao, Y.-G. Guo, S.-F. Zheng, X.-L. Wu, L.-Y. Jiang, R.-R. Bi, L.-J. Wan, J. Maier, Chem. Mater. 22 (2010) 1908–1914.
[10] G.F. Ortiz, I. Hanzu, P. Lavela, P. Knauth, J.L. Tirado, T. Djenizian, Chem. Mater. 22 (2010) 1926–1932.
[11] J.S. Chen, L.A. Archer, X. Wen Lou, J. Mater. Chem. 21 (2011) 9912.
[12] X.W. Lou, L.A. Archer, Z. Yang, Adv. Mater. 20 (2008) 3987–4019.
[13] X. Lai, J.E. Halpert, D. Wang, Energy Environ. Sci. 5 (2012) 5604–5618.
[14] B. Song, S. Liu, J. Jian, M. Lei, X. Wang, H. Li, J. Yu, X. Chen, J. Power Sources 180 (2008) 869–874.
[15] J. Wang, Y. Bai, M. Wu, J. Yin, W.F. Zhang, J. Power Sources 191 (2009) 614–618.
[16] J.S. Chen, X.W. Lou, Electrochem. Commun. 11 (2009) 2332–2335.
[17] M. Bousa, B. Laskova, M. Zukalova, J. Prochazka, A. Chou, L. Kavan, J. Electrochem. Soc. 157 (2010) A1108–A1112.
[18] S. Ding, J.S. Chen, Z. Wang, Y.L. Cheah, S. Madhavi, X. Hu, X.W. Lou, J. Mater. Chem. 21 (2011) 1677.
[19] J.S. Chen, Z. Wang, X.C. Dong, P. Chen, X.W. Lou, Nanoscale 3 (2011) 2158.
[20] H. Li, H. Zhou, Chem. Commun. 48 (2012) 1201–1217.

[21] U. Lafont, L. Simonin, M. Gaberscek, E.M. Kelder, J. Power Sources 174 (2007) 1104–1108.
[22] J. Kong, Z. Liu, Z. Yang, H.R. Tan, S. Xiong, S.Y. Wong, X. Li, X. Lu, Nanoscale 4 (2012) 525.
[23] X. Han, Q. Kuang, M. Jin, Z. Xie, L. Zheng, J. Am. Chem. Soc. 131 (2009) 3152–3153.
[24] X. Sun, J. Liu, Y. Li, Chem. Eur. J. 12 (2006) 2039–2047.
[25] X.H. Yang, Z. Li, C. Sun, H.G. Yang, C. Li, Chem. Mater. 23 (2011) 3486–3494.
[26] F. Tian, Y. Zhang, J. Zhang, C. Pan, J. Phys. Chem. C 116 (2012) 7515.
[27] A.S. Barnard, L.A. Curtiss, Nano Lett. 5 (2005) 1261.
[28] F.-F. Cao, X.-L. Wu, S. Xin, Y.-G. Guo, L.-J. Wan, J. Phys. Chem. C 114 (2010) 10308–10313.
[29] H.C. Choi, Y.M. Jung, S.B. Kim, Vib. Spectrosc. 37 (2005) 33–38.
[30] Q. Li, J. Zhang, B. Liu, M. Li, S. Yu, L. Wang, Z. Li, D. Liu, Y. Hou, Y. Zou, B. Zou, T. Cui, G. Zou, Cryst. Growth Des. 8 (2008) 1812–1814.

[31] F. Tuinstra, J.L. Koenig, J. Chem. Phys. 53 (1970) 1126.
[32] A. Ferrari, J. Robertson, Phys. Rev. B 64 (2001) 075414.
[33] C. Sun, L. Liu, L. Qi, H. Li, H. Zhang, C. Li, F. Gao, L. Dong, J. Colloid Interface Sci. 364 (2011) 288–297.
[34] A.-H. Lu, T. Sun, W.-C. Li, Q. Sun, F. Han, D.-H. Liu, Y. Guo, Angew. Chem. Int. Ed. 50 (2011) 11765–11768.
[35] J. Hassoun, P. Ochal, S. Panero, G. Mulas, C.B. Minella, B. Scrosati, J. Power Sources 180 (2008) 568.
[36] S. Yoon, A. Manthiram, J. Phys. Chem. C 115 (2011) 9410–9416.
[37] K.-H. Lee, S.-W. Song, ACS Appl. Mater. Interfaces 3 (2011) 3697–3703.
[38] X.-F. Zhang, K.-X. Wang, X. Wei, J.-S. Chen, Chem. Mater. 23 (2011) 5290–5292.
[39] Z. Wang, X.W.D. Lou, Adv. Mater. 24 (2012). http://dx.doi.org/10.1002/adma.201104546.
[40] Y. Wang, X. Su, S. Lu, J. Mater. Chem. 22 (2012) 1969.